minerals

MDPI

Article

Zircon LA-ICP-MS Dating and Geochemical Characteristics of Rhyolites from the Qushi Area, Tengchong Terrane, Yunnan Province

Xiong Mo [1,2], Chen Gong [1], Yan Shang [1], Jinglong Wu [1], Jialin Wu [2], Ronghui Qi [2], Xiaofeng Wang [3], Qi Guan [2] and Xu Kong [1,*]

[1] Ordos Institute of Technology, Ordos 017010, China
[2] Yunnan Institute of Geology Survey, Kunming 650216, China
[3] Yunnan Planning and Design Institute of Land Resources, Kunming 650216, China
* Correspondence: konx163@163.com

Abstract: The Qushi rhyolites, situated in the eastern sector of the Tengchong terrane, are critical to understanding the Early Cretaceous tectono-magmatic evolution of the Eastern Tethyan Tectonic Domain. Zircon LA-ICP-MS U-Pb geochronology indicates crystallization ages of 118.3–120.5 Ma, with Ti-in-zircon temperatures of 641–816 °C (mean = 716 °C), representing the Early Cretaceous magmatic activity in the Tengchong terrane. Inherited zircons within the rhyolites yield a zircon age of ca. 198.5 Ma, with corresponding Ti-in-zircon temperatures of 615–699 °C (mean = 657 °C), implying the potential presence of an Early Jurassic igneous basement beneath the Qushi region. Geochemically, the rhyolites are classified as calc-alkaline and weakly to moderately peraluminous (A/CNK = 1.07–2.86). These rocks display signatures typical of acidic magmas, marked by significant enrichments in light rare earth elements (LREE: La and Ce) and large ion lithophile elements (LILE: Rb, K, Th and U) while simultaneously exhibiting depletions in high-field-strength elements (HFSE: Nb, Ta, Ti, and P) and heavy rare earth elements (HREE). Trace element signatures further reveal marked depletions in Sr (12.4–244.7 ppm) and Ba while displaying enrichments in Zr and Hf. These geochemical features, including the huge range of the Sr content and A/CNK ratios, suggest both I-type and S-type granite affinities. The Early Cretaceous volcanism of the Qushi rhyolites is likely attributed to the combined effects of subduction and the closure of the Meso-Tethyan Ocean (MTO). This volcanic activity is interpreted to result from subduction-related processes associated with the MTO, potentially involving slab rollback, slab break-off, and subsequent asthenospheric upwelling. The formation of these rhyolites may also be linked to the final closure of the MTO, characterized by the Late Cretaceous collision and amalgamation of the Burma and Tengchong terranes.

Keywords: zircon U–Pb ages; rhyolites; Qushi area; Tengchong terrane; Yunnan province

check for updates

Academic Editors: Ilya Bindeman and Ming Wang

Received: 19 February 2025
Revised: 11 March 2025
Accepted: 14 March 2025
Published: 18 March 2025

Citation: Mo, X.; Gong, C.; Shang, Y.; Wu, J.; Wu, J.; Qi, R.; Wang, X.; Guan, Q.; Kong, X. Zircon LA-ICP-MS Dating and Geochemical Characteristics of Rhyolites from the Qushi Area, Tengchong Terrane, Yunnan Province. *Minerals* **2025**, *15*, 315. https://doi.org/10.3390/min15030315

Copyright: © 2025 by the authors. Licensee MDPI, Basel, Switzerland. This article is an open access article distributed under the terms and conditions of the Creative Commons Attribution (CC BY) license (https://creativecommons.org/licenses/by/4.0/).

1. Introduction

The Eastern Tethyan Tectonic Domain (ETTD), situated between the Eurasian Plate and the Indian Plate, records a prolonged geodynamic evolution spanning approximately 400 million years [1]. This domain preserves critical evidence of multi-stage tectonic processes, including the rifting of Gondwana-derived terranes, the opening and closure of the Neo-Tethyan Ocean (NTO), and subsequent continental collision and accretionary orogenesis; thus, it has attracted substantial attention from tectonic and igneous geologists [2–9].

The ETTD comprises a series of accreted crustal blocks (including the Himalayan, Songpan–Ganzi, Lhasa, and Qiangtang terranes) separated by the Indus–Yarlung, Bangong–Nujiang, and Jinsha suture zones (Figure 1a) [6,10,11]. Although paleomagnetic evidence indicates that the Lhasa block underwent a ca. 87° clockwise rotation during the Eocene (ca. 40 Ma), tectonic correlation analyses confirm its structural kinship with the Tengchong terrane in the southeastern ETTD [12,13].

Robust evidence from the Lhasa terrane confirms voluminous Mesozoic magmatic activity, supported by comprehensive geochronological and petrogenetic analyses [2,14–16]. The magmatism in the Lhasa terrane can be categorized into three distinct stages. The first stage, occurring between 140 and 120 Ma, is characterized by calc-alkaline granites [15,16], potentially related to the southward subduction of the Bangong–Nujiang oceanic crust beneath the Lhasa terrane [15,17]. The second stage, spanning 118 to 110 Ma, includes granitoids and volcanic rocks, with granitoids being widely distributed within the Lhasa terrane. This phase may be associated with slab break-off of the Bangong–Nujiang oceanic crust [2,14,15,18,19]. The third stage, during the Late Cretaceous (94 to 72 Ma), is marked by granitic rocks, which may be the result of the delamination of the lower crust of the central–northern Lhasa terrane after the collision of the Lhasa and Qiangtang terranes [20–24].

Compared with the Lhasa terrane, the Jurassic–Cretaceous magmatic activity in the Tengchong terrane remains controversial. The igneous activities spanning the Triassic to Jurassic periods in the Tengchong terrane are scattered across the region (Figure 1b). The Early–Middle Triassic igneous events (250–236 Ma) might have resulted from partial melting of the thickened lower crust after the Tengchong and Baoshan terranes collided and merged. The Late Triassic igneous events (219–213 Ma) could be related to the collision with the Indochina terrane [25]. Additionally, the Early Jurassic magmatic events (198–180 Ma) in the Tengchong terrane could be linked to the subduction of the Meso-Tethys Ocean and the collision between the Tengchong terrane and Eurasian continent [25], or they could have formed in the post-collisional tectonic setting response to the Paleo-Tethyan regime [26]. The Early Cretaceous magmatic events have been ascribed to two primary mechanisms: (1) the development of post-collisional arc systems linked to the subduction of the Meso-Tethyan oceanic crust [27–29]; and (2) flat subduction processes of the far-field Neo-Tethyan oceanic crust. The geological environment of the Late Cretaceous magmatic events have been variably attributed to (1) syn-collisional [30,31] or (2) extensional settings [32,33]. The Tengchong terrane may exhibit a spatially westward migration pattern with three high-magma-addition-rate events during the Early Cretaceous (ca. 131–111 Ma), Late Cretaceous to Early Cenozoic (ca. 76–64 Ma), and Early Cenozoic (ca. 55–49 Ma) [11,34]. Notably, the Early Cenozoic (55–49 Ma) magmatic episode may correlate with slab break-off following the initial India–Asia collision [11,35].

Therefore, establishing further constraints on the Cretaceous tectono-magmatic events of this region is crucial, and as an important component of the southeastern ETTD, the Tengchong terrane consists of various Early and Late Cretaceous magmatic rocks and offers valuable clues to constrain the Early and Late Cretaceous tectono-magmatic events. This study focuses on rhyolites from the Qushi area of the Tengchong terrane, and an integrated investigation, including field geological mapping, petrographic observations, and zircon LA-ICP-MS U-Pb geochronology, was conducted. These multidisciplinary approaches aim to provide more data on Early Cretaceous magmatic events and advance our understanding of southeastern ETTD's Mesozoic tectono-magmatic evolution.

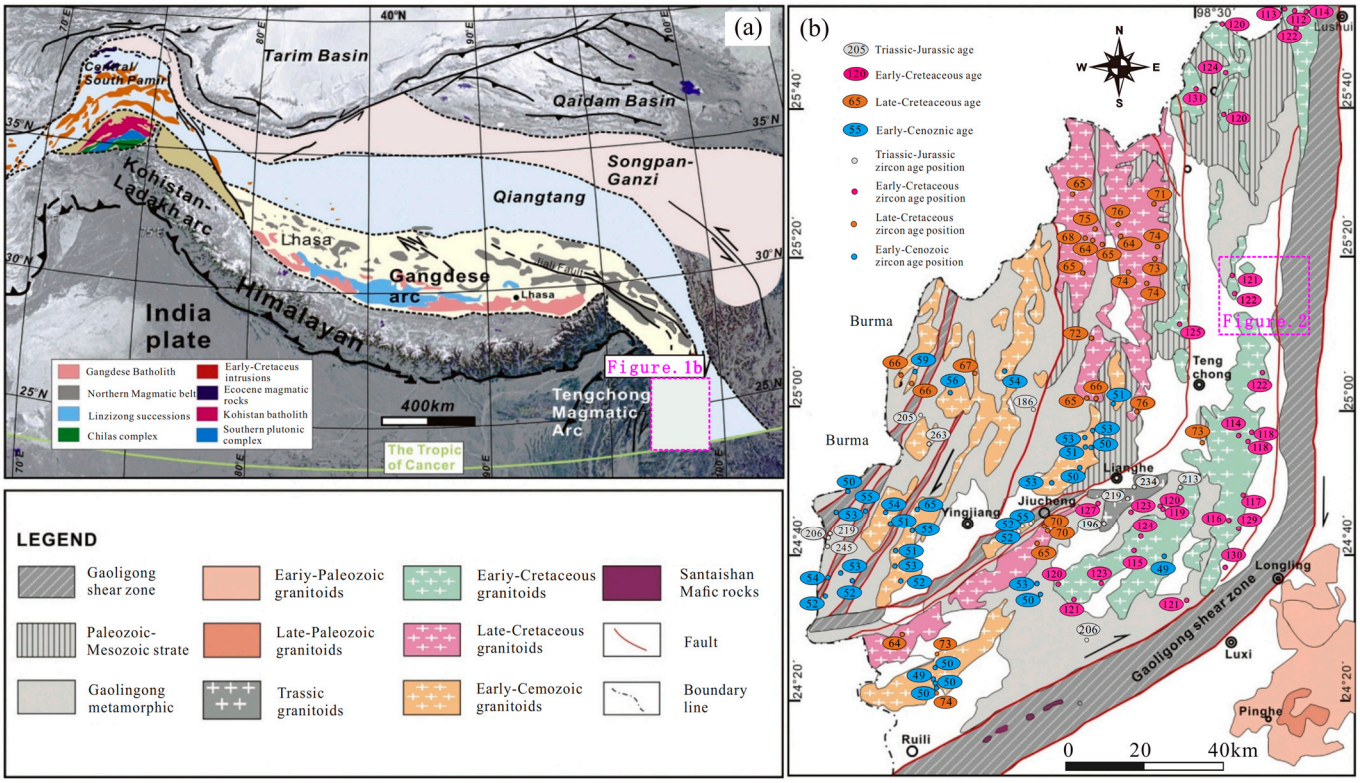


Figure 1. (**a**) Generalized main continental blocks in the ETTD and the positions of the Tengchong terrane (modified after [11,36,37]). (**b**) Schematic regional geological map of the Tengchong area illustrating the distribution of the Mesozoic igneous rocks (modified after [5,6,11,13,34,37,38]).

2. Geological Setting

The study area is located in Qushi town, north of Tengchong city, which is part of the eastern Tengchong terrane, with the Gaoligong shear zone to the east (Figure 1b). The stratigraphic sequence in the study area mainly comprises the Neoproterozoic Meijiashan Group, Permian, and Triassic strata (Figure 2). The Meijiashan Group is subdivided into four formations: the Jiuduhe Formation, Danlonghe Formation, Baohuashan Formation, and Erdaohe Formation. The Permian Bangdu Formation consists of silty slate, while the Triassic Hewanjie Formation is characterized by dolomite and dolomitic limestone. The Neogene Mangbang Formation is composed of sandstone, conglomerate, and claystone. Quaternary basalts are extensively distributed along the western margin of the study area, representing the southwestern extension of the Tengchong Volcanic Belt. Intrusive rocks are predominantly Late Jurassic to Early Cretaceous granitoids. NNE-trending fault structures are well developed in the eastern part of the study area, transecting distribution zone of the Meijiashan Group and inducing mylonitization of the host rocks.

This study focused on rhyolites (originally assigned to the Erdaohe Formation of the Meijiashan Rock Group, [39]) from the Sunjiaying and Xinqiao villages in the Qushi area of the Tengchong terrane (Figures 1b, 2 and 3). Five representative samples were collected and used for comprehensive petrographic, geochemical, and isotopic geochronological analyses. Detailed sampling information such as rock types, GPS locations, and mineral assemblages are systematically listed in Table S1.

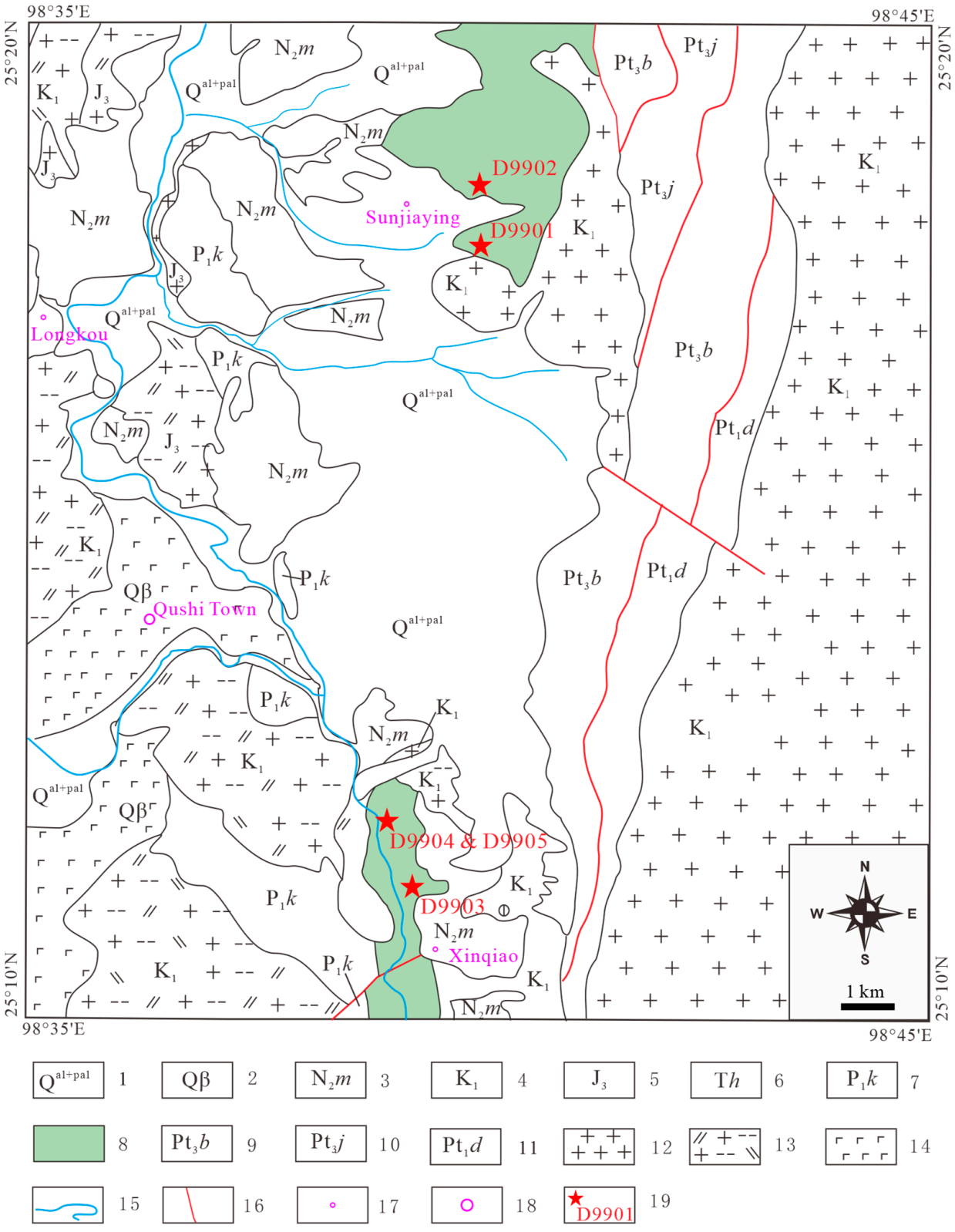


Figure 2. Geological sketch map of the Qushi area (modified after [39]). 1. Quaternary alluvial and proluvial deposits; 2. Quaternary basalt; 3. Mangbang Formation; 4. Early Cretaceous granite; 5. Late Jurassic monzogranite; 6. Triassic Hewanjie Formation; 7. Permian Kongshuhe Formation; 8. Rhyolites; 9. Baohuashan Formation; 10. Jiuduhe Formation; 11. Shanlonghe Formation; 12. granite; 13. biotite monzogranite; 14. basalt; 15. geological boundary; 16. fault; 17. village; 18. town; 19. sampling locations.

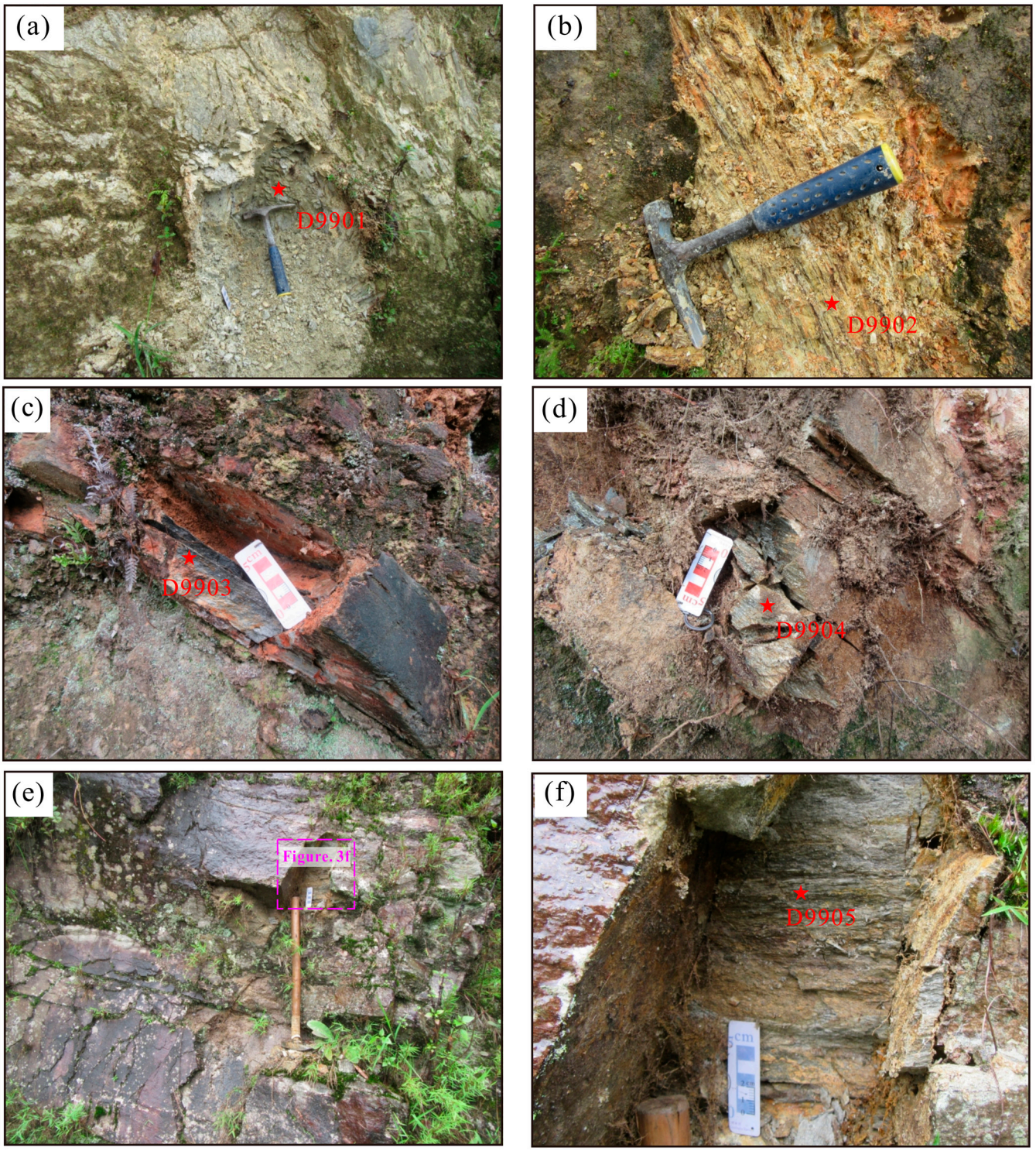


Figure 3. Field photos of the rhyolites for sample D9901 (**a**), D9902 (**b**), D9903 (**c**), D9904 (**d**), and D9905 (**e**,**f**) in the Qushi area.

3. Samples and Analytical Methods

3.1. Geochemical Analysis

Geochemical analyses were executed at the Yunnan Institute of Geological Survey to establish the major and trace element compositions of rhyolites. Major elements were measured via X-ray fluorescence (XRF), while trace elements (including REEs) were analyzed with inductively coupled plasma mass spectrometry (ICP-MS). Trace element concentrations were adjusted relative to chondritic and primitive mantle values following [40]'s

method. The analytical precision obtained was within ±5% for major elements and within ±10% for trace elements.

3.2. Zircon U-Pb Dating and Trace Element Analysis

Zircon U-Pb dating via LA-ICP-MS (laser ablation inductively coupled plasma mass spectrometry) was executed at Wuhan Sample Solution Analytical Technology Co., Ltd. in Wuhan, China. The detailed operational conditions for the laser ablation system and ICP-MS instrument, as well as data reduction procedures, are presented in [41]. Laser sampling utilized a GeolasPro laser ablation system, which included a COMPexPro 102 ArF excimer laser (Lambda Physik, Göttingen, Germany; 193 nm wavelength, 200 mJ maximum energy) and a MicroLas optical system. An Agilent 7900 ICP-MS instrument was employed to measure ion signal intensities. Helium was applied as the carrier gas, and argon functioned as the make-up gas, combined with the carrier gas via a T-connector prior to entering the ICP torch. A signal smoothing device, known as the "wire" device, was incorporated into the laser ablation system to enhance signal stability [42]. In this study, the laser spot size was set to 24 μm, and the repetition rate was 6 Hz. For U-Pb dating, zircon 91,500 was used as the external calibration standard [43]. Each analysis included a background acquisition period of approximately 20–30 s to measure the gas blank, followed by 50 s of data acquisition from the sample. The trace element compositions of zircon were calibrated using NIST 610 glass (National Institute of Standards & Technology, Gaithersburg, MD, USA) as an external calibration. The Excel-based software ICPMSDataCal (version 9.5) was utilized for offline data reduction, enabling the selection and integration of background and analytical signals, time-drift correction, and quantitative calibration for U-Pb dating and trace element analysis [44,45]. Weighted mean age calculations and concordia diagrams were generated utilizing Isoplot/Ex version 3.0 [46]. A total of 93 spots were analyzed across three samples (D9901, D9902, D9904) with $^{206}Pb/^{238}U$ ages (Table S4). Ti-in-zircon thermometry was calculated using the calibration of [47] (Table S5).

4. Results

4.1. Petrography Characteristics

The rhyolites exhibited prominent flow banding structures, characterized by strongly oriented microcrystals within the matrix, which may be associated with lava flow during rapid cooling processes (Figure 4a–c), and they exhibited a homogeneous porphyritic texture with a glassy to cryptocrystalline groundmass (Figure 4a–f). These rhyolites were mainly composed of mineral assemblages of quartz (Qz, 30–50 vol.%, 200–1500 μm in length), potassium feldspar (Kfs, 20–35 vol.%, euhedral-to-subhedral crystals, 500–3000 μm in length), and minor plagioclase (Pl, 5–15 vol.%). biotite (Bt, 2–6 vol.%) and magnetite (Mag, 1–3 vol.%) were also present, along with accessory minerals such as apatite (Ap) and zircon (Zr) (Table S1; Figure 4). Under plane-polarized light, the quartz phenocrysts displayed resorbed boundaries, indicating magmatic resorption processes.

4.2. Geochemical Features

In the Al_2O_3 vs. TiO_2 discrimination diagram, these samples fell within the field of acidic igneous rocks (Figure 5a) [48,49]. In the Nb/Y vs. Zr/TiO_2 diagram, they were plotted in the rhyodacite/dacite or trachyte–andesite fields (Figure 5b) [50]. The A/NK ratios of the Qushi rhyolites ranged from 1.61 to 1.75, with occasional values up to 2.91. All A/CNK values exceeded 1.0 (Table S2), indicating weakly peraluminous to peraluminous characteristics. The Rittmann index (σ43) varied between 0.96 and 1.72 (Table S2), classifying these rocks as calc-alkaline rhyolites.

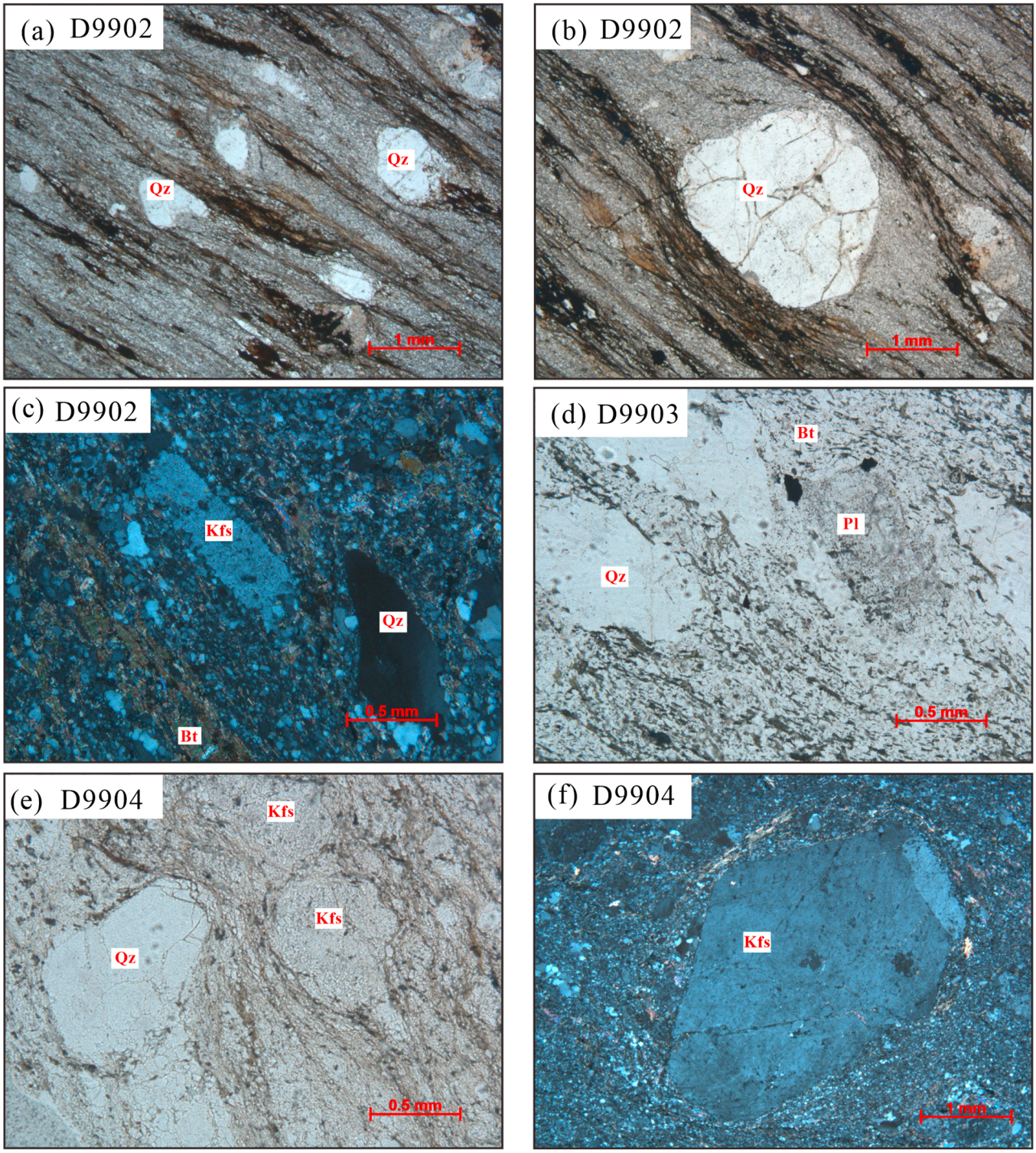


Figure 4. Representative photomicrographs of rhyolites for samples D9902 (**a**–**c**), D9903 (**d**), and D9904 (**e**,**f**) from the Qushi area. (**a**–**e**) Photomicrographs taken under plane-polarized light; (**c**,**f**) photomicrographs taken under cross-polarized light. Qz—quartz, Kfs—potassium feldspar, Bt—biotite, Pl—plagioclase.

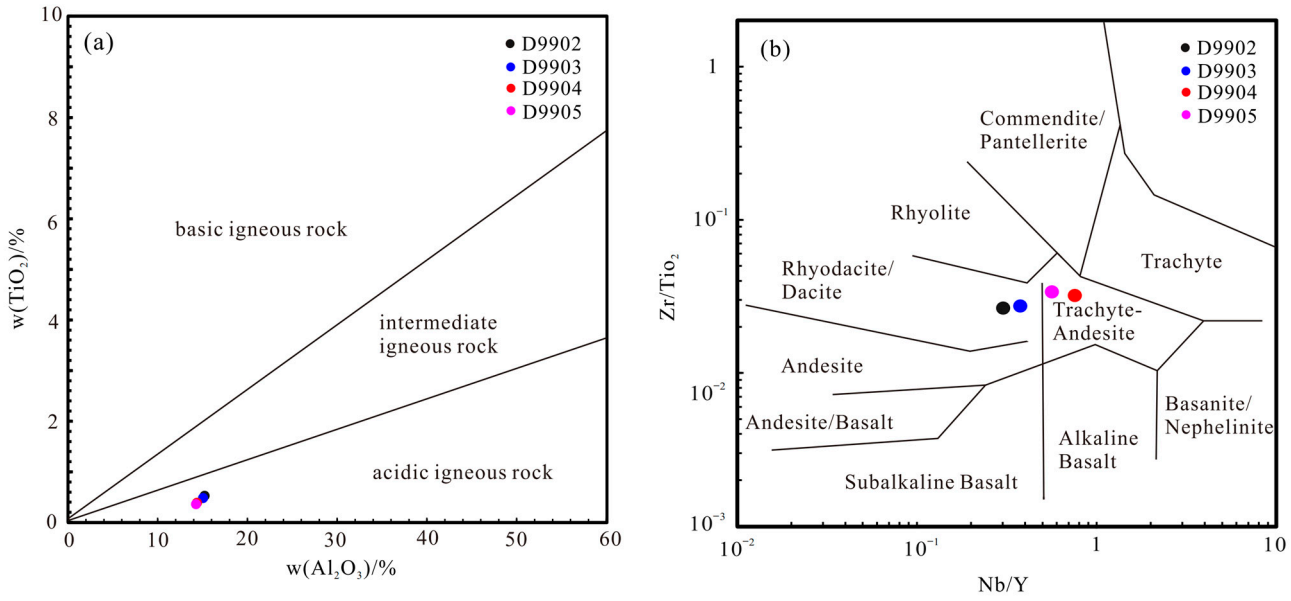


Figure 5. Discrimination diagram of rhyolites in the Qushi area. (**a**) TiO_2 versus Al_2O_3 diagram (modified after [48,49]); (**b**) Zr/TiO_2 versus Nb/Y diagram (modified after [50]).

The total rare earth element (ΣREE) concentrations of the Qushi rhyolites ranged from 173 to 195 ppm. Their LREE/HREE ratios varied between 7.6 and 14.9, while the La_N/Yb_N ratios ranged from 9.8 to 18.5. The δEu and δCe values ranged from 0.69 to 0.76 and 0.48 to 1.01, respectively (Table S3). Chondrite-normalized REE patterns exhibited uniformly right-sloping trends with mid-REE "V"-shaped troughs (Figure 6a).

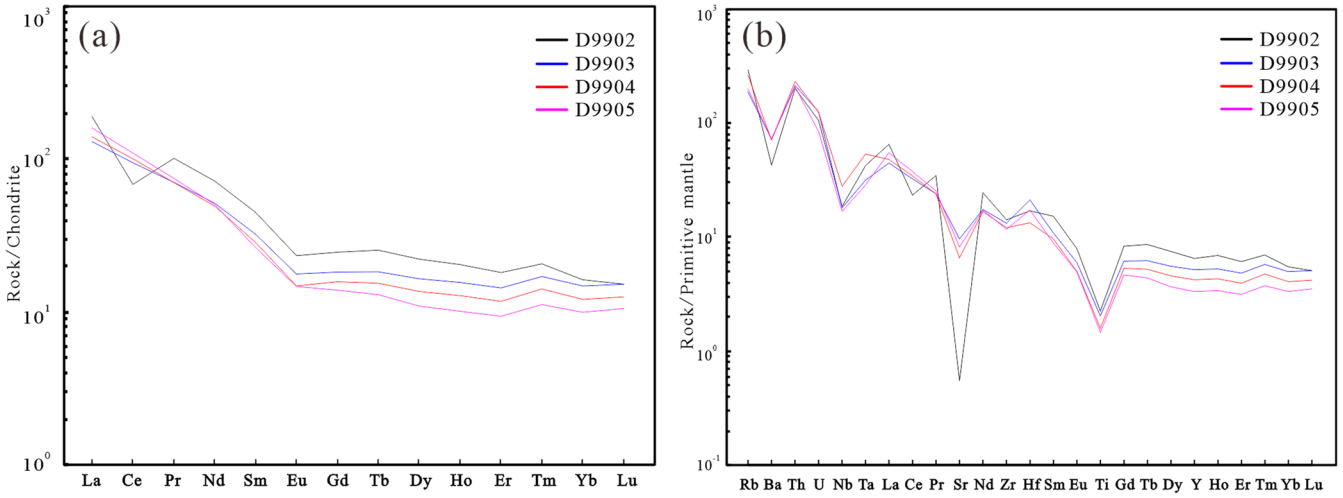


Figure 6. (**a**) Chondrite-normalized REE for the rhyolites from the Qushi area; (**b**) Primitive-mantle-normalized trace element patterns for the rhyolites from the Qushi area. The values for chondrite and primitive mantle are from [40].

Primitive-mantle-normalized trace element spider diagrams displayed a right-sloping "M"-type multi-peak pattern. This pattern shows significant enrichment in large-ion lithophile elements (LILEs: Rb, K), radiogenic elements (Th, U), and magmaphile elements (Ce, La, Zr, Hf). There were also marked negative anomalies in high-field-strength elements (HFSEs: Nb, Ta, P, Ti) and some LILEs (Sr, Ba) (Figure 6b).

4.3. Zircon U-Pb Geochronology

Zircon grains from sample D9901 were predominantly euhedral-to-subhedral prismatic, with rare subangular or fragmented grains. Their lengths ranged from 50 to 100 μm (rarely exceeding 100 μm), and their aspect ratios ranged from 1:1 to 2:1. Cathodoluminescence (CL) images revealed distinct oscillatory zoning in all zircons (Figure 7a). Due to significant radiogenic Pb loss, spots 1, 4, 5, 6, 14, 18, 20, 22, and 26 were excluded (Table S4). The remaining analytical spots yielded Th and U concentrations of 125–751 ppm and 100–1027 ppm, respectively, with Th/U ratios of 0.73–1.47 (Table S4). These zircons displayed a chondrite-normalized rare earth element (REE) pattern characterized by light REE (LREE) depletion, heavy REE (HREE) enrichment, and pronounced negative δEu anomalies (Figure 8a). The magmatic nature of these zircons was confirmed by their concordant ($^{206}U/^{208}Pb$) ages of 118–124 Ma, with a weighted mean age of 120.5 ± 1.2 Ma (MSWD = 2.2, n = 17; Table S4, Figure 8a,b). This age was interpreted as the crystallization age of the rhyolite.



Figure 7. Cathodoluminescence images labeled with $^{206}Pb/^{238}U$ ages of the zircons separated from rhyolites (**a**–**c**). The yellow numbers are the analytical spot symbols, the red numbers are the respective ages ($^{206}U/^{208}Pb$ ages were used when the zircon age was less than 1000 Ma), and the red circle stands for 24 μm.

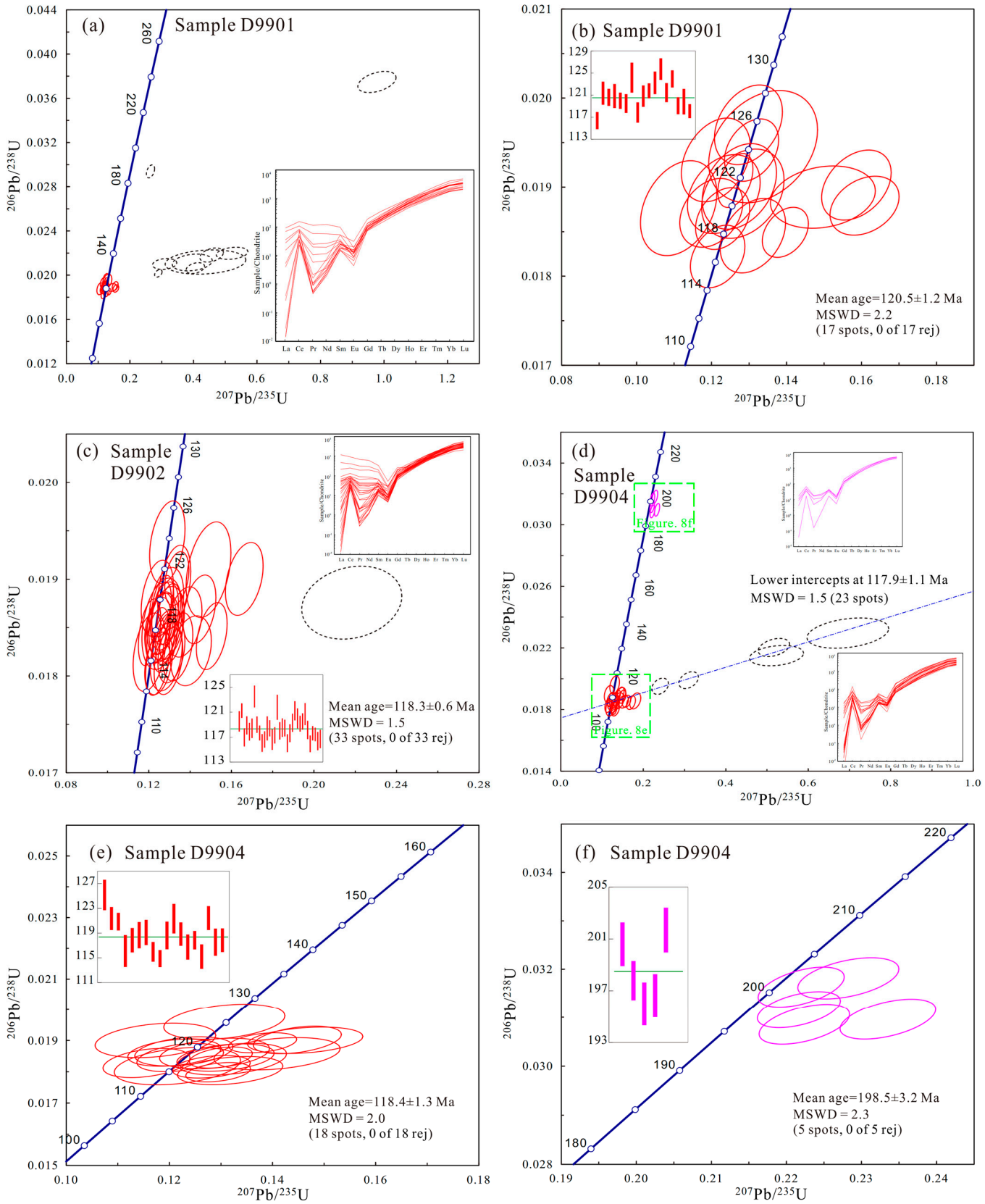


Figure 8. Concordia diagrams, chondrite-normalized rare-earth element patterns, and histograms of Cenozoic ages for the magmatic zircons of rhyolites. (The red circles denote individual zircon analyses from the ca. 120 Ma sample, while the pink circles represent zircon analyses from the ca. 200 Ma sample. The red bar delineates the ca. 120 Ma age range of the younger sample, whereas the pink bar illustrates the ca. 200Ma span of the older sample.) Chondrite values are from [40]. (**a**) Concordia diagram for Sample D9901, showing the distribution of 206Pb/238U and 207Pb/235U

ratios. (**b**) Concordia diagram for Sample D9901 with age histograms and mean age calculation. (**c**) Concordia diagram for Sample D9902. (**d**) Concordia diagram for Sample D9904 with age histograms and mean age calculation. (**e**) Concordia diagram for Sample D9904 with age histograms and mean age calculation. (**f**) Concordia diagram for Sample D9904 with age histograms and mean age calculation.

Zircons from sample D9902 were predominantly euhedral-to-subhedral prismatic or pyramidal crystals, with rare irregular grains. The grain lengths ranged from 100 to 150 μm (rarely exceeding 150 μm), with aspect ratios of 2:1 to 5:1. CL imaging showed well-developed oscillatory zoning (Figure 7b). Excluding spot 7 due to radiogenic Pb loss (Table S4), the remaining spots yielded Th and U concentrations of 129–738 ppm and 167–1165 ppm, respectively, with Th/U ratios of 0.44–1.09 (Table S4). Their REE patterns exhibited LREE depletion, HREE enrichment, and marked negative δEu anomalies (Figure 8c). The magmatic zircons yielded $^{206}U/^{208}Pb$ ages of 116–120 Ma, with a weighted mean age of 118.3 ± 0.6 Ma (MSWD = 1.5, n = 33; Table S4, Figure 8c), representing the crystallization age of the rhyolite.

Zircons from sample D9904 were divided into two groups based on CL characteristics. Group 1 (including spots 6, 15, 23, 27, and 33) were predominantly elongated prisms (50–100 μm in length, with aspect ratios of 1:1 to 3:1, Figure 7c). Their REE patterns showed LREE depletion, HREE enrichment, and strong negative δEu anomalies (Figure 8d). The Th and U concentrations ranged from 792.7 to 1922.2 ppm and 2228 to 3786 ppm, respectively, with Th/U ratios of 0.29 to 0.63. These zircons yielded magmatic U-Pb ages of 183–205 Ma, with a weighted mean age of 198.5 ± 3.2 Ma (MSWD = 2.3, n = 5; Table S4, Figure 8f), interpreted as inherited/captured zircons from an older magmatic source. Group 2 (excluding spots 2, 3, 7, 10, 13, 16, 17, 24, and 28 due to radiogenic Pb loss; Table S4) displayed light CL images, with grain lengths of 50 to 150 μm (rarely exceeding 150 μm) and aspect ratios of 1:1 to 4:1. Their REE patterns also showed LREE depletion, HREE enrichment, and negative δEu anomalies (Figure 8d). The Th and U concentrations ranged from 83.9 to 1089.9 ppm and 121.7 to 530.8 ppm, respectively, with Th/U ratios of 0.29 to 1.69. A lower intercept age of 117.9 ± 1.1 Ma was obtained (Figure 8d), with magmatic U-Pb ages clustering at 112–128 Ma and a weighted mean age of 118.4 ± 1.3 Ma (MSWD = 2, n = 18; Table S4, Figure 8e). This age was interpreted as the crystallization age of the rhyolite.

5. Discussion

5.1. Cretaceous Magmatism in Tengchong Terrane

The Cretaceous magmatic activity in the Tengchong terrane is a significant stage in the Mesozoic tectono-magmatic evolution of the southeastern ETTD. Zircon LA-ICP-MS U-Pb dating of the Qushi rhyolite gave crystallization ages ranging from 120.5 ± 1.2 Ma to 118.3 ± 0.6 Ma, in agreement with Early Cretaceous magmatic events documented in the Tengchong terrane [6,11,25,51,52]. Contemporaneous intrusive and extrusive rocks have been identified throughout the Tengchong terrane.

The study area and its surrounding regions contain monzogranite, syenite, and rhyolite, with ages spanning 104–125 Ma. Specifically, (1) the monzogranites exhibit zircon U-Pb ages of 120–122 Ma [6]; (2) the syenites yield ages of 104–120 Ma [53]; and (3) the rhyolites display ages of 116–125 Ma [54].

The northern region of Tengchong terrane (north of the study area) contains granodiorites, granites, and monzogranites with distinct age clusters. (1) The granodiorites at 120 km north of the study area are 117–125 Ma [30]; (2) the granites at 100 km north of the study area are 115–125 Ma [55]; (3) the northeastern granites (140 km of the study area) are

122–128 Ma [56]; (4) the northern granites (130 km of the study area) are 115–129 Ma [57]; and (5) the monzogranite porphyries (130 km north of the study area) are 120–123 Ma [58].

The western and southern areas of the Tengchong terrane include diverse lithologies. (1) The monzogranites (a) 20 km west of the study area are 113–128 Ma, and (b) those 50 km south of the study area are 114–122 Ma [59]; (2) the quartz diorites (70 km southwest of the study area) are 123.7–130.2 Ma [60]; (3) the quartz monzonites are 121–129 Ma [61]; (4) the granites (60 km southwest of the study area) are 117–131 Ma [55]; (5) the monzonites and syenogranites (70 km south of the study area) are 113–126 Ma [57]; and (6) the granodiorites (80 km south of the study area) are 110–126 Ma [62].

5.2. Rhyolite and Its Petrogenesis

Early Cretaceous magmatic activities were extensively distributed across the Tengchong terrane (130–111Ma, peak at ca. 120 Ma) [25]. In the northern part of the Tengchong terrane, Early Cretaceous granites are mainly high-K calc-alkaline, whereas those in the southern part are medium-K calc-alkaline. These Early Cretaceous granites of the Tengchong terrane exhibit metaluminous-to-peraluminous characteristics, displaying high LREE/HREE and $(La/Yb)_N$ ratios, along with negative Eu anomalies ([25] and its internal references). Compared with Early Cretaceous granites reported by other studies, the Qushi rhyolites are classified as acidic high-K calc-alkaline igneous rocks with REE patterns of strong LREE enrichment and heavy REE depletion with moderately negative Eu anomalies, suggesting crustal melting with plagioclase fractional crystallization. These geochemical features, including strong LREE enrichment, HREE depletion, moderate negative Eu anomalies, and localized weak negative Ce anomalies, suggest a crustal melting-dominated origin with plagioclase fractional crystallization. Coupled with their calc-alkaline and peraluminous characteristics, these data imply magma generation through crustal melting or crust–mantle interaction in a subduction-related tectonic setting. Thus, the geochemical characteristics of the Qushi rhyolite may be closer to the granites in the northern part of the Tengchong terrane.

Prior studies indicate that the dominant rocks of the Early Cretaceous granites of the Tengchong terrane exhibit I-type or highly fractionated I-type granites, with minor S-type granites [6,25,63]. In I-type and S-type granite discrimination diagrams, the Qushi rhyolites span both I-type and S-type granite fields (Figure 9) [52]. Sample D9902 exhibited an A/CNK value of 2.86 (significantly >1.1) along with an extremely low Sr content of 12.4 ppm (significantly <100 ppm) and lower Mg# value of 0.279. In contrast, samples D9903, D9904, and D9905 showed A/CNK ratios ranging from 1.07 to 1.18, with elevated Sr concentrations between 163.8 and 244.7 ppm (all >100 ppm) and higher Mg# values (0.306–0.353) (Table S2). These distinct geochemical signatures suggest that sample D9902 likely represents S-type granite, while samples D9903, D9904, and D9905 may belong to I-type granite [64].

Most of the Early Cretaceous granitoids in northern region of the Tengchong terrane may originated from basaltic magmas, and the minor S-type granitoids in northern region exhibit sedimentary affinities, predominantly originating from argillaceous protoliths [6,25,30,58]. Multiple petrogenetic studies propose that the Early Cretaceous magmatic systems in Tengchong terrane may represent hybrid crust–mantle sources, as evidenced by isotopic signatures and mineralogical assemblages [27,29,54,59,63,65–68]. In the southern part of the Tengchong terrane, the Early Cretaceous granitoids display features typical of a volcanic arc origin, whereas the northern region's granitoids demonstrate collisional origin properties [25]. The occurrence of mafic enclaves in both the southern and northern areas indicates a potential gradual rise in mantle-derived magma during the Early Cretaceous period [25,59,62,63,65–67,69].

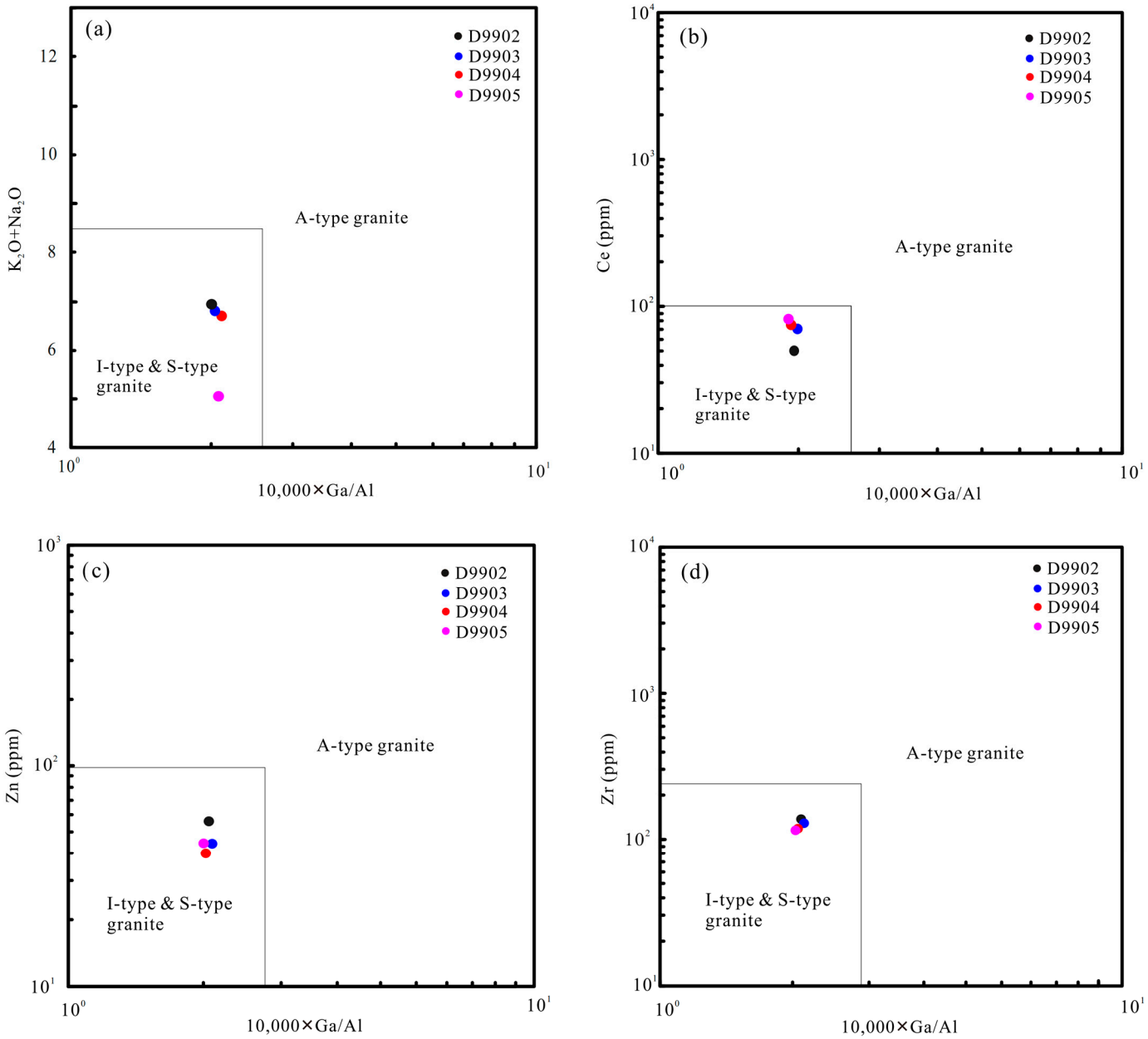


Figure 9. I-type and S-type granite discrimination diagram for the rhyolites from the Qushi area (after [51]). Geochemical classification diagrams for granitic samples. (**a**) K_2O + Na_2O vs. 10,000 × Ga/Al diagram, showing the distribution of samples D9902, D9903, D9904, and D9905. The diagram distinguishes A-type granite from I-type and S-type granite. (**b**) Ce vs. 10,000 × Ga/Al diagram, illustrating the geochemical characteristics of the samples and their classification into A-type or I-type & S-type granite. (**c**) Zr vs. 10,000 × Ga/Al diagram, further differentiating the granitic samples based on their geochemical properties. (**d**) Another Zr vs. 10,000 × Ga/Al diagram, providing additional insights into the classification and geochemical features of the samples.

The A/MF vs. C/MF diagram (Figure 10d) shows that the Qushi rhyolite samples of D9903, D9904, and D9905 may have originated from the partial melt of meta-tonalitic or meta-greywacke, while sample D9902 may have originated from a meta-pelitic source [70]. In the Rb/Sr vs. Rb/Ba diagram (Figure 10e), the samples D9903, D9904, and D9905 of the rhyolites were plotted in a shale or greywacke source, and sample D9902 was plotted in a pelite-derived melt [71]. The igneous source of the Qushi rhyolites align with those reported by Qi et al. (2020) from the neighboring region (Figure 10d,e) [54]. The presence of inherited zircon grains of ca. 198.5 Ma in the Qushi region (Figure 8f) suggests a polygenetic

origin for the parent magmas of the rhyolites. This includes contributions from lower-crustal mafic meta-igneous components, meta-sedimentary materials, and minor inputs from mantle-derived sources, with potential contributions from some arc-related materials.

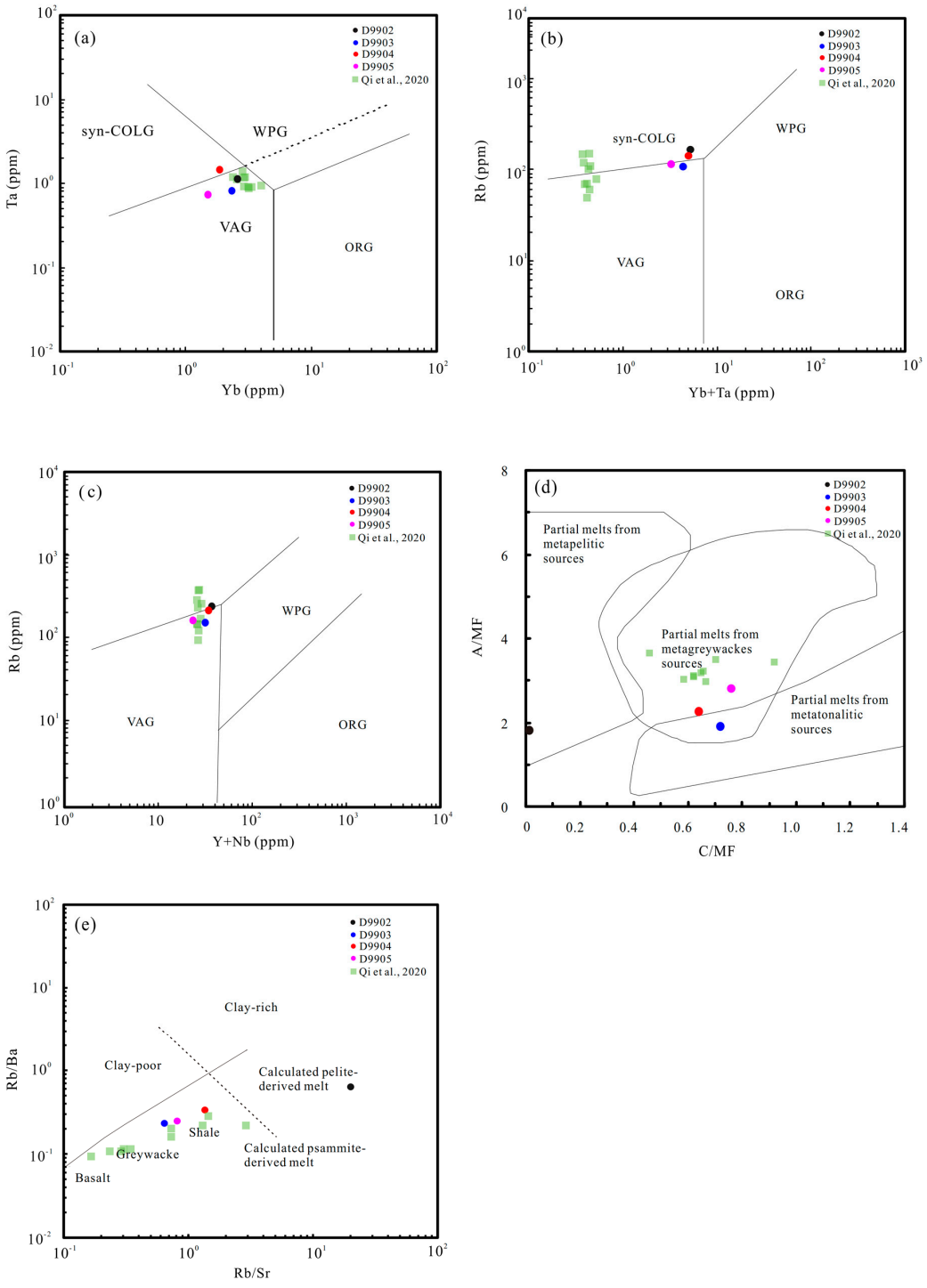


Figure 10. The discrimination diagrams of tectonic setting (after [72]). (**a**) Ta vs. Yb, (**b**) Rb vs. Yb + Ta, and (**c**) Rb vs. Y + Nb discrimination diagrams of tectonic setting. (**d**) A/MF vs. C/MF discrimination diagrams of magma sources (after [70]), A/MF = molar $Al_2O_3/(MgO + TFeO)$, C/MF: molar CaO/(MgO + TFeO). (**e**) Rb/Ba vs. Rb/Sr discrimination diagram for the rhyolites from the Qushi area and [54] (after [71]).

5.3. Tectonic Significance

The Qushi rhyolites were formed at 118.3–120.5 Ma with Ti-in-Zr temperatures of 641–816 °C (average = 716 °C), representing Early Cretaceous magmatism in the Tengchong terrane (Figures 8, 11c and 12). The inherited zircon ages of ca. 198.5 Ma (615–699 °C, average = 657 °C) (Figures 8, 11c and 12) suggest that Early Jurassic igneous units may be present in the basement of the Qushi region. Previous studies indicate that the zircon saturation temperatures for magmatic activities of 198–180 Ma (Tzr < 750 °C) are significantly lower than those for magmatic activities of 130–111 Ma (Tzr > 800 °C) in the Tengchong terrane [25], which is roughly consistent with this study. The Early Jurassic magmatism of S-type granites in the Tengchong terrane may have formed in the tectonic background of a syn-collision or post-collision environment linked to the collision between the Tengchong terrane and the Eurasian continent [6,25,26,53].

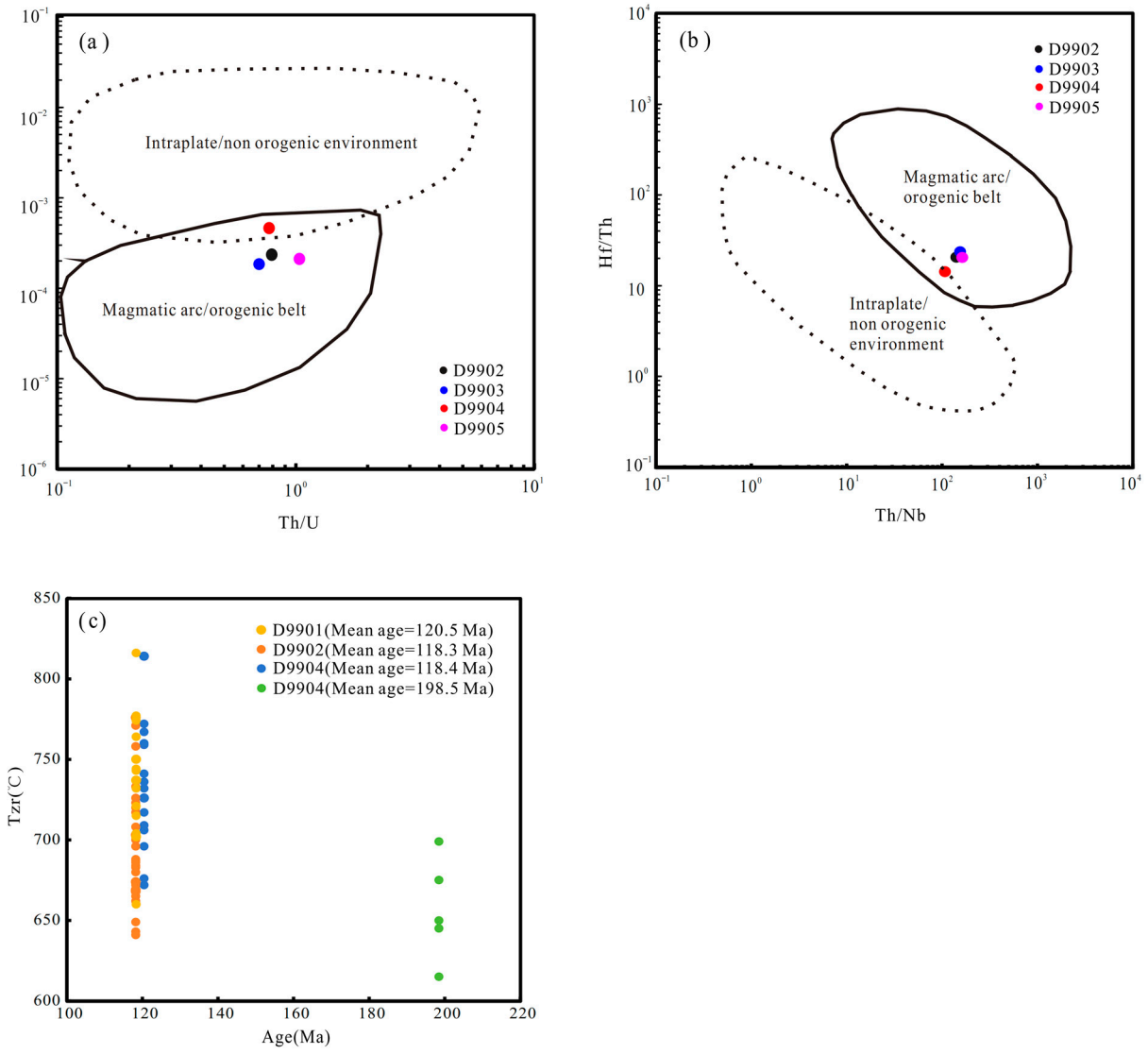


Figure 11. Magmatic zircon trace element discriminating diagrams of rhyolites in the Qushi area (after [73,74]). (**a**) Th/U vs. Nb/Hf, (**b**) Th/Nb vs. Hf/Th discrimination diagrams of tectonic setting. (**c**) Rhyolites Ti-in-Zr temperatures [47]. WPG = within-plate granite, VAG = volcanic arc granite, post-COLG = post-collision granite, syn-COLG = syn-collisional granite, ORG = ocean ridge granite.

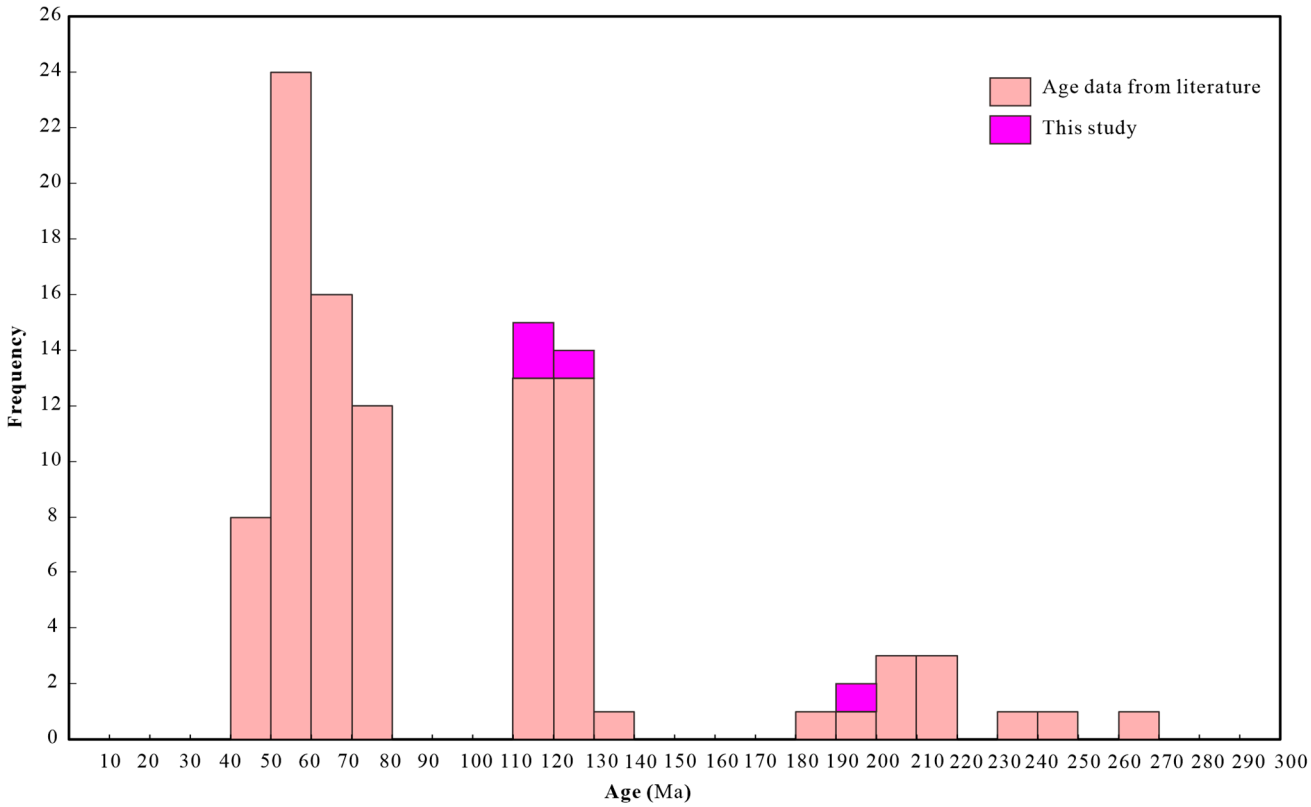


Figure 12. Histogram of reported magmatic zircon ages from the Tengchong terrane. Data sourced from the same as Figure 1b.

In relation to the Early Cretaceous magmatic activities, six unique tectonic models have been proposed for the Tengchong terrane, including (1) an arc setting related to the NTO flat subducted eastward beneath the Tengchong terrane, followed by rollback of the subducted slab [62,69,75–79]; (2) a magmatic arc setting linked to northward (eastward) subduction of the MTO crust beneath the Tengchong terrane [6,27–29,63,66,80–83]; (3) a post-collisional tectonic setting of crustal thickening related to the closure of the MTO [30,58]; (4) southward subduction of the MTO beneath the Tengchong terrane [28,29,53,65,67,68]; (5) the slab break-off of the MTO beneath the Tengchong terrane linked to the closure of the Meso-Tethyan Ocean [28,59,66]; and (6) the north-to-south scissor-shaped closure of the MTO [25].

On the tectonic discrimination diagrams (Figure 10a–c), the rhyolites were plotted within the volcanic arc granite (VAG) and syn-collisional granite (syn-COLG) fields, indicating a subduction-related setting. In addition, on the tectonic discrimination diagrams (Figure 11a–b), the rhyolites were plotted within the magmatic arc and orogenic belt, indicating a subduction-related compression setting. Considering the MTO was situated between the Tengchong and Burma terranes and still open between 130–111 Ma [6,63,81], it is unlikely that the Early Cretaceous magmatism was triggered by the subduction of the NTO or affected by the southward (westward) subduction of the MTO. Bimodal volcanic rocks of ca. 120 Ma formed in a back-arc basin system have been discovered in Baoshan terrane and indicate that the magmatic arc may be present in the Tengchong terrane [78]. Furthermore, previous studies suggest that the collision between the Burma terrane and the Tengchong terrane may have occurred during the Cretaceous period [6,63,81,84]. Yang et al. (2024) proposed that the MTO's north-to-south scissor-shaped closure may have triggered the Early Cretaceous magmatism of the Tengchong terrane [25]; however, due to limited regional data, additional evidence is required to validate this hypothesis.

In conclusion, the formation of the Qushi rhyolite may be related to the subduction, slab rollback, slab break-off, and upwelling of the asthenosphere associated with the MTO, and it may also be linked with the final closure of the MTO (the collision and malgamation of the Burma terrane and the Tengchong terrane) (Figure 13).

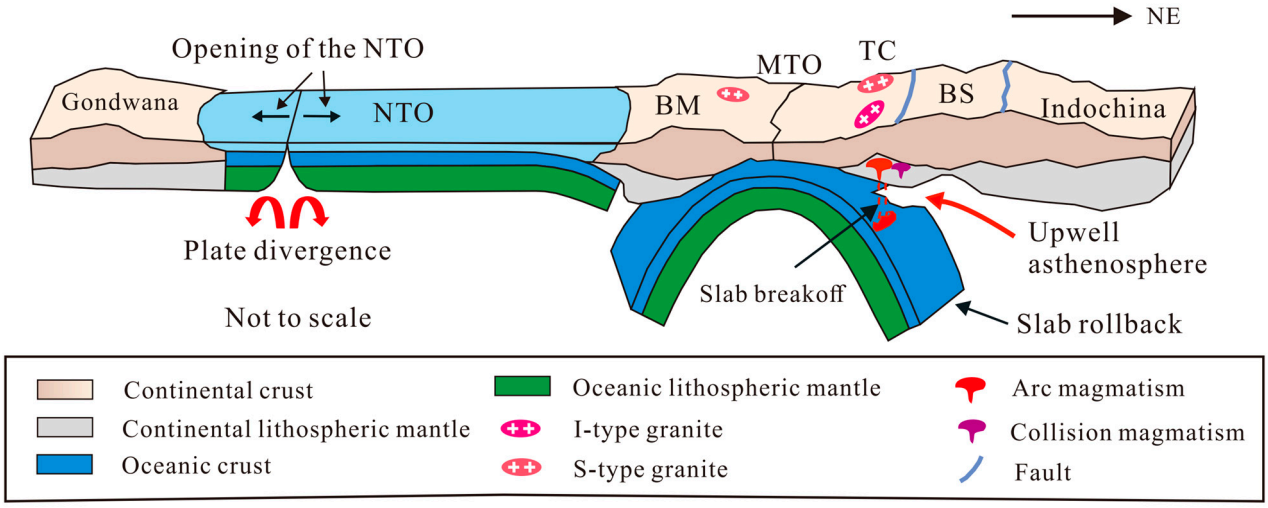


Figure 13. Conceptual frameworks illustrating the Early Cretaceous geodynamic evolution of the Tengchong terrane (modified after [25]). TC: Tengchong terrane, BS: Baoshan terrane, PTO: Paleo-Tethys Ocean, BM: Burma terrane, NTO: Neo-Tethys Ocean, MTO: Meso-Tethys Ocean.

(1) Zircon LA-ICP-MS U-Pb dating indicates that the Qushi rhyolites were crystallized from 118.3 Ma to 120.5 Ma, representing Early Cretaceous magmatic activity in the Tengchong terrane. Additionally, the rhyolites contain inherited zircon ages of approximately 198.5 Ma, suggesting the potential presence of Early Jurassic igneous units in the basement of the Qushi region.

(2) The Qushi rhyolites are classified as acidic, calc-alkaline rhyolites with weakly peraluminous-to-peraluminous characteristics and exhibit petrogeochemical characteristics of enrichment in LREE, Rb, K, Th, U, Ce, La, Zr and Hf and depletion of HREE, Nb, Ta, P, Ti, Sr and Ba.

(3) The A/CNK values of the Qushi rhyolites range from 1.07 to 2.86, alongside Sr content variations from 12.4 to 244.7 ppm, suggest both I-type and S-type granite affinities, indicative of crustal melting with plagioclase fractionation.

(4) The Qushi rhyolites probably formed in syn-COLG and VAG tectonic settings related to the combined effects of the subduction and the closure of the MTO.

Supplementary Materials: The following supporting information can be downloaded at: https://www.mdpi.com/article/10.3390/min15030315/s1, Table S1: Sample numbers, rock types, GPS locations, and mineral assemblages of the rocks in this study. The mineral abbreviations are derived from [85]; Table S2: Analysis results of major elements of rhyolites from the Qushi area. A/NK = $Al_2O_3/(Na_2O + K_2O)$ (mol); A/CNK = $Al_2O_3/(CaO + Na_2O + K_2O)$ (mol); σ43 = $(Na_2O + K_2O)^2/(SiO_2\text{-}43)$(Wt%); A/MF = $Al_2O_3/(TFeO + MgO)$ (mol); C/MF = $CaO/(TFeO + MgO)$ (mol); Mg# = $MgO/(MgO + TFeO)$ (mol); Table S3: Analysis results of trace elements of rhyolites from the Qushi area; Table S4: LA-ICP-MS U–Pb isotope data for zircons of rhyolites from the Qushi area; Table S5: Trace element data for zircons of rhyolites from the Qushi area. Ti-in-Zr temperatures were calculated based on [47].

Author Contributions: X.M. and C.G. equally contributed to the work, and they are joint first authors. Conceptualization, X.K.; methodology, X.M. and C.G.; validation, X.M., C.G. and X.K.; formal analysis, X.M.; investigation, X.M., J.W. (Jialin Wu), R.Q., X.W. and Q.G.; resources, X.M.; data curation, X.M., C.G. and X.K.; writing—original draft preparation, X.M. and C.G.; writing—review and editing, X.K., Y.S. and J.W. (Jinglong Wu); supervision, X.K.; funding acquisition, X.K., Y.S. and X.M. All authors have read and agreed to the published version of the manuscript.

Funding: This work was supported by the High-level Talent Scientific Research Start-Up Fund of Ordos (grant number: DC2400001462), Ordos Mining Area Geohazard Prevention and Geoenvironmental Protection Engineering Research Center (grant number: RZ2300001544), Planning and Management of Paleontological Fossil Conservation in Yunnan Province (project number: 530000210000000021416), and 1:50,000 Scale Regional Geological Survey of six geological maps including Dongpengyang in Yunnan Province (project number: D2017012).

Data Availability Statement: Data are contained within the article or Supplementary Materials.

Acknowledgments: We extend our sincere gratitude to Jing Li from the Yunnan Geological Survey for their enthusiastic help and assistance during the fieldwork of this study. We sincerely thank Ming Wang for their helpful discussions in improving the quality of this paper. We also thank two anonymous reviewers for their constructive comments.

Conflicts of Interest: The authors declare no conflicts of interest.

References

1. Metcalfe, I. Gondwana dispersion and Asian accretion: Tectonic and palaeogeographic evolution of eastern Tethys. *J. Asian Earth Sci.* **2013**, *66*, 1–33. [CrossRef]
2. Zhu, D.C.; Mo, X.; Niu, Y.; Zhao, Z.; Wang, L.; Liu, Y.; Wu, F. Geochemical investigation of Early Cretaceous igneous rocks along an east–west traverse throughout the central Lhasa Terrane, Tibet. *Chem. Geol.* **2009**, *268*, 298–312. [CrossRef]
3. Hou, Z.; Zhang, H. Geodynamics and metallogeny of the eastern Tethyan metallogenic domain. *Ore Geol. Rev.* **2015**, *70*, 346–384. [CrossRef]
4. Hu, X.; Garzanti, E.; Wang, J.; Huang, W.; An, W.; Webb, A.A. The timing of India-Asia collision onset–Facts, theories, controversies. *Earth-Sci. Rev.* **2016**, *160*, 264–299. [CrossRef]
5. Cao, H.-W.; Zhang, Y.-H.; Santosh, M.; Zhang, S.-T.; Tang, L.; Pei, Q.-M. Mineralogy, zircon U–Pb–Hf isotopes, and whole-rock geochemistry of Late Cretaceous–Eocene granites from the Tengchong terrane, western Yunnan, China: Record of the closure of the Neo-Tethyan Ocean. *Geol. J.* **2017**, *52*, 1423–1441. [CrossRef]
6. Cao, H.; Zhang, Y.; Tang, L.; Hollis, S.P.; Zhang, S.; Pei, Q.; Yang, C.; Zhu, X. Geochemistry, zircon U–Pb geochronology and Hf isotopes of Jurassic-Cretaceous granites in the Tengchong terrane, SW China: Implications for the Mesozoic tectono-magmatic evolution of the Eastern Tethyan Tectonic Domain. *Int. Geol. Rev.* **2019**, *61*, 257–279. [CrossRef]
7. Kong, X.; Mi, W.; Zhu, L.; Yang, W. Zircon U-Pb chronology and provenance of the Paleogene sandstones in the Nima basin, Tibet: Implication for coeval paleogeography. *Arab. J. Geosci.* **2019**, *12*, 692. [CrossRef]
8. Zhu, D.C.; Wang, Q.; Zhao, Z.D.; Chung, S.L.; Cawood, P.A.; Niu, Y.; Mo, X.X. Magmatic record of India-Asia collision. *Sci. Rep.* **2015**, *5*, 14289. [CrossRef] [PubMed]
9. Qi, X.X.; Sheng, H.; Wei, C.; Ren, Y.F.; Cai, Z.H.; Ji, F.B.; Liang, F.; Liu, X. Longlin-Ruili subduction-accretionary complex belt in the southeastern Gaoligong orogen, and its relationship with the evolution of the Meso-Tethyan Ocean. *Acta Petrol. Sin.* **2021**, *37*, 3067–3094. (In Chinese with English abstract)
10. Yin, A.; Harrison, T. Geologic Evolution of the Himalayan-Tibetan Orogen. *Annu. Rev. Earth Planet. Sci.* **2000**, *28*, 211–280. [CrossRef]
11. Zhu, R.Z.; Lai, S.; Paterson, S.R.; Luffi, P.; Zhang, B.; Pompe, L.R. Westward migration of high-magma addition rate events in SE Tibet. *Tectonophysics* **2022**, *807*, 229096. [CrossRef]
12. Kornfeld, D.; Eckert, S.; Appel, E.; Ratschbacher, L.; Sonntag, B.; Pfänder, J.A.; Ding, L.; Liu, D. Cenozoic clockwise rotation of the Tengchong block, southeastern Tibetan Plateau: A paleomagnetic and geochronologic study. *Tectonophysics* **2014**, *628*, 105–122. [CrossRef]
13. Xu, Z.Q.; Wang, Q.; Cai, Z.H.; Dong, H.W.; Li, H.Q.; Chen, X.J.; Duan, X.D.; Cao, H.; Li, J.; Burg, J.-P. Kinematics of the Tengchong terrane in SE Tibet from the Late Eocene to Early Miocene: Insights from coeval mid-crustal detachments and strike-slip shear zones. *Tectonophysics* **2015**, *665*, 127–148. [CrossRef]

14. Qu, X.X.; Wang, R.; Xin, H.; Jiang, J.; Chen, H. Age and petrogenesis of A-type granites in the middle segment of the Bangonghu–Nujiang suture, Tibetan plateau. *Lithos* **2012**, *146–147*, 264–275. [CrossRef]
15. Chen, Y.; Zhu, D.; Zhao, Z.; Meng, F.; Wang, Q.; Santosh, M.; Wang, L.; Dong, G.; Mo, X. Slab breakoff triggered ca. 113 Ma magmatism around Xainza area of the Lhasa Terrane, Tibet. *Gondwana Res.* **2014**, *26*, 449–463.
16. Li, F.; Tang, J.; Wang, N.; Liu, Z.; Song, Y.; Zhang, J.; Ma, X.; Fu, B.; Li, H.; Han, S. Petrogenesis and Geodynamic Implications of Early Cretaceous (∼130 Ma) Magmatism in the Baingoin Batholith, Central Tibet: Products of Subducting Slab Rollback. *Acta Geol. Sin. (Engl. Ed.)* **2022**, *96*, 1960–1978. [CrossRef]
17. Zhu, D.C.; Zhao, Z.; Niu, Y.; Mo, X.; Chung, S.; Hou, Z.; Wang, L.; Wu, F. The Lhasa Terrane: Record of a microcontinent and its histories of drift and growth. Earth Planet. *Sci. Lett.* **2011**, *301*, 241–255.
18. Mi, W.T.; Kong, X.; Zhang, D.; Hu, J.; Wan, Y. Zircon LA-ICP-MS dating and geochemical characteristics of I-type granitoids from the Yanhu area, west segment of the Bangongco-Nujiang suture (western Tibet): Petrogenesis and implications for the southward subduction of the Tethyan Ocean. *J. Geol. Soc. India* **2017**, *90*, 335–346. [CrossRef]
19. Ma, X.; Song, Y.; Tang, J.; Chen, W. Newly identified rhyolite-biotite monzogranite (A2-type granite)-norite belt from the Bangong-Nujiang collision zone in Tibet Plateau: Evidence for the slab break-off beneath the Lhasa Terrane. *Lithos* **2020**, *366–367*, 105565. [CrossRef]
20. Li, Y.; He, J.; Wang, C.; Santosh, M.; Dai, J.; Zhang, Y.; Wei, Y.; Wang, J. Late Cretaceous K-rich magmatism in central Tibet: Evidence for early elevation of the Tibetan plateau? *Lithos* **2013**, *160*, 1–13. [CrossRef]
21. Wang, Q.; Zhu, D.; Zhao, Z.; Liu, S.; Chung, S.; Li, S.; Liu, D.; Dai, J.; Wang, L.; Mo, X. Origin of the ca. 90 Ma magnesia-rich volcanic rocks in SE Nyima, central Tibet: Products of lithospheric delamination beneath the Lhasa-Qiangtang collision zone. *Lithos* **2014**, *198*, 24–37. [CrossRef]
22. Chen, J.; Xu, J.; Yu, H.; Wang, B.; Wu, J.; Feng, Y. Late Cretaceous high-Mg# granitoids in southern Tibet: Implications for the early crustal thickening and tectonic evolution of the Tibetan Plateau? *Lithos* **2015**, *232*, 12–22.
23. Yi, J.; Wang, Q.; Zhu, D.; Li, S.; Liu, S.; Wang, R.; Zhang, L.L.; Zhao, Z. Westward-younging high-Mg adakitic magmatism in central Tibet: Record of a westward-migrating lithospheric foundering beneath the Lhasa–Qiangtang collision zone during the Late Cretaceous. *Lithos* **2018**, *316*, 92–103. [CrossRef]
24. Sun, M.; Tang, J.; Chen, W.; Ma, X.; Qu, X.; Song, Y.; Li, X.; Ding, J. Process of lithospheric delamination beneath the Lhasa–Qiangtang collision orogen: Constraints from the geochronology and geochemistry of Late Cretaceous volcanic rocks in the Lhasa terrane, central Tibet. *Lithos* **2020**, *356*, 10529. [CrossRef]
25. Yang, X.; Zhang, Z.; Zhou, Y.; Yang, J. Spatio-temporal analysis of Permian-Cretaceous magmatic activities in the Tengchong block: Implications for its tectono-magmatic evolution. *Geosci. Front.* **2024**, *15*, 101920. [CrossRef]
26. Wang, G.; Liu, Z.; Tan, S.; He, X.; Wang, Y.; Qi, C.; Ye, H. Petrogenesis of the Early Jurassic Longtang and Menglong Peraluminous Granites in Tengchong Terrane, and their Tectonic Implication. *Acta Geol. Sin. (Engl. Ed.)* **2022**, *96*, 1079–1990. [CrossRef]
27. Zhu, R.Z.; Lai, S.; Qin, J.; Zhao, S. Early-Cretaceous highly fractionated I-type granites from the northern Tengchong block, western Yunnan, SW China: Petrogenesis and tectonic implications. *J. Asian Earth Sci.* **2015**, *100*, 145–163. [CrossRef]
28. Zhu, R.Z.; Lai, S.; Qin, J.; Zhao, S. Petrogenesis of late Paleozoic-to-early Mesozoic granitoids and metagabbroic rocks of the Tengchong Block, SW China: Implications for the evolution of the eastern Paleo-Tethys. *Int. J. Earth Sci.* **2017**, *107*, 431–457. [CrossRef]
29. Zhao, S.; Lai, S.; Qin, J.; Zhu, R. Tectono-magmatic evolution of the Gaoligong belt, southeastern margin of the Tibetan plateau: Constraints from granitic gneisses and granitoid intrusions. *Gondwana Res.* **2016**, *35*, 238–256. [CrossRef]
30. Xu, Y.G.; Yang, Q.J.; Lan, J.B.; Luo, Z.Y.; Huang, X.L.; Shi, Y.R.; Xie, L.W. Temporal-spatial distribution and tectonic implications of the batholiths in the Gaoligong-Tengliang-Yingjiang area, western Yunnan: Constraints from zircon U-Pb ages and Hf isotopes. *J. Asian Earth Sci.* **2012**, *53*, 151–175. [CrossRef]
31. Qi, X.; Zhu, L.; Grimmer, J.C.; Hu, Z. Tracing the Transhimalayan magmatic belt and the Lhasa block southward using zircon U–Pb, Lu–Hf isotopic and geochemical data: Cretaceous—Cenozoic granitoids in the Tengchong block, Yunnan, China. *J. Asian Earth Sci.* **2015**, *110*, 170–188. [CrossRef]
32. Chen, X.; Hu, R.; Bi, X.; Zhong, H.; Lan, J.; Zhao, C.; Zhu, J. Petrogenesis of metaluminous A-type granitoids in the Tengchong–Lianghe tin belt of southwestern China: Evidences from zircon U–Pb ages and Hf–O isotopes, and whole-rock Sr–Nd isotopes. *Lithos* **2015**, *212*, 93–110. [CrossRef]
33. Zhao, S.; Lai, S.; Qin, J.; Zhu, R.; Wang, J. Geochemical and geochronological characteristics of Late Cretaceous to Early Paleocene granitoids in the Tengchong Block, Southwestern China: Implications for crustal anatexis and thickness variations along the eastern Neo-Tethys subduction zone. *Tectonophysics* **2017**, *694*, 87–100. [CrossRef]
34. Cao, H.; Zou, H.; Zhang, Y.H.; Zhang, S.T.; Zheng, L.; Zhang, L.K.; Tang, L.; Pei, Q.-M. Late Cretaceous magmatism and related metallogeny in the Tengchong area: Evidence from geochronological, isotopic and geochemical data from the Xiaolonghe Sn deposit, western Yunnan, China. *Ore Geol. Rev.* **2016**, *78*, 196–212. [CrossRef]

35. Bouilhol, P.; Jagoutz, O.; Hanchar, J.M.; Dudas, F.O. Dating the India–Eurasia collision through arc magmatic records. *Earth Planet. Sci. Lett.* **2013**, *366*, 163–175. [CrossRef]
36. Chung, S.; Chu, M.F.; Zhang, Y.; Xie, Y.; Lo, C.H.; Lee, T.Y.; Lan, C.Y.; Li, X.; Zhang, Q.R.; Wang, Y. Tibetan tectonic evolution inferred from spatial and temporal variations in post-collisional magmatism. *Earth-Sci. Rev.* **2005**, *68*, 173–196. [CrossRef]
37. Chapman, J.B.; Scoggin, S.H.; Kapp, P.A.; Carrapa, B.; Ducea, M.; Worthington, J.R.; Oimahmadov, I.; Gadoev, M. Mesozoic to Cenozoic magmatic history of the Pamir. *Earth Planet. Sci. Lett.* **2018**, *482*, 181–192. [CrossRef]
38. Zhao, S.; Fang, X.; Tai, W.; Lai, S.; Pei, X.; Li, Z. Origin of granitic magma within continental margin arc magmatic lull: Constraints by the Late Cretaceous granites in Tengchong Block, SE Tibet. *Acta Petrol. Sin.* **2025**, *41*, 91–111, (In Chinese with English abstract).
39. Yunnan Institute of Geological Sciences (YIGS). *Regional Geological Survey Report of the Qushijie, Dajujie, and Dadongjie Areas at 1:50,000 Scale, Yunnan Province*; Yunnan Institute of Geological Sciences: Kunming, China, 2004. (In Chinese)
40. Sun, S.S.; McDonough, W.F. Chemical and isotopic systematics of oceanic basalts: Implications for mantle composition and processes. *Geol. Soc. Spec. Pub.* **1989**, *42*, 313–345. [CrossRef]
41. Zong, K.; Klemd, R.; Yuan, Y.; He, Z.Y.; Guo, J.L.; Shi, X.L.; Liu, Y.S.; Hu, Z.C.; Zhang, Z.M. The assembly of Rodinia: The correlation of early Neoproterozoic (ca. 900 Ma) high-grade metamorphism and continental arc formation in the southern Beishan Orogen, southern Central Asian Orogenic Belt (CAOB). *Precambrian Res.* **2017**, *290*, 32–48. [CrossRef]
42. Hu, Z.C.; Zhang, W.; Liu, Y.S.; Gao, S.; Li, M.; Zong, K.Q.; Chen, H.H.; Hu, S.H. "Wave" signal-smoothing and mercury-removing device for laser ablation quadrupole and multiple collector ICPMS analysis: Application to lead isotope analysis. *Anal. Chem.* **2015**, *87*, 1152–1157. [CrossRef] [PubMed]
43. Hu, Z.C.; Li, X.H.; Luo, T.; Zhang, W.; Crowley, J.; Li, Q.L.; Ling, X.X.; Yang, C.; Li, Y.; Feng, L.P.; et al. Tanz zircon megacrysts: A new zircon reference material for the microbeam determination of U–Pb ages and Zr–O isotopes. *J. Anal. At. Spectrom.* **2021**, *36*, 2715–2734. [CrossRef]
44. Liu, Y.S.; Hu, Z.C.; Gao, S.; Günther, D.; Xu, J.; Gao, C.G.; Chen, H.H. In situ analysis of major and trace elements of anhydrous minerals by LA-ICP-MS without applying an internal standard. *Chem. Geol.* **2008**, *257*, 34–43. [CrossRef]
45. Liu, Y.S.; Gao, S.; Hu, Z.C.; Gao, C.G.; Zong, K.Q.; Wang, D.B. Continental and oceanic crust recycling-induced melt-peridotite interactions in the Trans-North China Orogen: U-Pb dating, Hf isotopes and trace elements in zircons of mantle xenoliths. *J. Petrol.* **2010**, *51*, 537–571. [CrossRef]
46. Ludwig, K.R. *ISOPLOT 3.00: A Geochronological Toolkit for Microsoft Excel*; Berkeley Geochronology Center: Berkeley, CA, USA, 2003; Volume 4, pp. 1–70.
47. Ferry, J.M.; Watson, E.B. New thermodynamic models and revised calibrations for the Ti-in-zircon and Zr-in-rutile thermometers. *Contr. Mineral. Petrol.* **2007**, *154*, 429–437. [CrossRef]
48. Hayashi, K.; Fujisawa, H.; Holland, H.D.; Ohmoto, H. Geochemistry of ~1.9 Ga sedimentary rocks from northeastern Labrador, Canada. *Geochim. Cosmochim. Acta* **1997**, *61*, 4115–4137. [CrossRef]
49. He, B.; Zhong, Y.; Xu, Y.; Li, X. Triggers of Permo-Triassic boundary mass extinction in South China: The Siberian Traps or Paleo-Tethys ignimbrite flare-up? *Lithos* **2014**, *204*, 258–267. [CrossRef]
50. Winchester, J.A.; Floyd, P.A. Geochemical discrimination of different magma series and their differentiation products using immobile elements. *Chem. Geol.* **1977**, *20*, 325–343. [CrossRef]
51. Cao, H.; Zhang, Y.H.; Pei, Q.M.; Zhang, R.Q.; Tang, L.; Lin, B.; Cai, G.J. U–Pb dating of zircon and cassiterite from the Early Cretaceous Jiaojiguan iron-tin polymetallic deposit, implications for magmatism and metallogeny of the Tengchong area, western Yunnan, China. *Int. Geol. Rev.* **2017**, *59*, 234. [CrossRef]
52. Whalen, J.B.; Currie, K.L.; Chappell, B.W. A-type granites: Geochemical characteristics, discrimination and petrogenesis. *Contr. Mineral. Petrol.* **1987**, *95*, 407–419. [CrossRef]
53. Zhu, R.Z.; Lai, S.C.; Qin, J.; Zhao, S. Early-Cretaceous Syenites and Granites in the Northeastern Tengchong Block, SW China: Petrogenesis and Tectonic Implications. *Acta Geol. Sin. Engl. Ed.* **2018**, *92*, 1349–1365. [CrossRef]
54. Qi, X.; Shen, H.; Ren, Y.; Wei, C.; Cai, Z.; Zhang, C.; Ji, F.; Liang, F. Early Cretaceous volcanism in the northwestern Gaoligong orogen and its relationship with subduction of the Nujiang Ocean: Evidence from geochemistry, zircon U-Pb dating and Hf isotopic compositions of rhyolites. *Acta Petrol. Sin.* **2020**, *36*, 2946–2962. (In Chinese with English abstract)
55. Yu, L. Genesis and Tectonic Significance of the Mesozoic Granitoids in the Tengchong-Baoshan Block, Sanjiang Area. Ph.D. Thesis, China University of Geosciences, Beijing, China, 2016; 137p.
56. Ma, X.; Shu, L.; Meert, J.G.; Li, J. The paleozoic evolution of central tianshan: Geochemical and geochronological evidence. *Gondwana Res.* **2014**, *25*, 797–819. [CrossRef]
57. Zhou, S.M. Petrogenesis of the Late Triassic-Early Eocene Granitoids in the Tengchong Block. Ph.D. Thesis, China University of Geosciences, Beijing, China, 2019; 168p. (In Chinese).
58. Cao, H.; Zhang, S.T.; Lin, J.Z.; Zheng, L.; Wu, J.D.; Li, D. Geology, geochemistry and geochronology of the Jiaojiguanliangzi Fe-polymetallic deposit, Tengchong County, Western Yunnan (China): Regional tectonic implications. *J. Asian Earth Sci.* **2014**, *81*, 142–152. [CrossRef]

59. Xie, J.C.; Zhu, D.C.; Dong, G.C.; Zhao, Z.D.; Wang, Q.; Mo, X.X. Linking the Tengchong Terrane in SW Yunnan with the Lhasa Terrane in southern Tibet through magmatic correlation. *Gondwana Res.* **2016**, *39*, 217–229. [CrossRef]
60. Li, Z.H.; Lin, S.L.; Cong, F.; Xie, T.; Zou, G.F. U-Pb ages of zircon from metamorphic rocks of the Gaoligongshan Group in western Yunnan and its tectonic significance. *Acta Petrol. Sin.* **2012**, *28*, 1529–1541. (In Chinese with English abstract)
61. Qi, X.X.; Zhu, L.H.; Hu, Z.C.; Li, Z.Q. Zircon SHRIMP U-Pb dating and Lu-Hf isotopic composition for Early Cretaceous plutonic rocks in Tengchong block, southeastern Tibet, and its tectonic implications. *Acta Petrol. Sin.* **2011**, *27*, 3409–3421. (In Chinese with English abstract)
62. Cong, F.; Lin, S.; Zou, G.; Li, Z.; Xie, T.; Peng, Z.; Liang, T. Magma mixing of granites at Lianghe: In-situ zircon analysis for trace elements, U-Pb ages and Hf isotopes. *Sci. China Earth Sci.* **2011**, *54*, 1346–1359. [CrossRef]
63. Fang, Y.; Zhang, Y.; Zhang, S.; Cao, H.; Zou, H.; Dong, J. Early Cretaceous I-type granites in the Tengchong terrane: New constraints on the late Mesozoic tectonic evolution of southwestern China. *Geosci. Front.* **2018**, *9*, 459–470. [CrossRef]
64. Chappell, B.W.; White, A.J. Two contrasting granite types. *J. Geol. Soc. Aust.* **1974**, *21*, 353–369.
65. Zhu, R.Z.; Lai, S.; Santosh, M.; Qin, J.; Zhao, S. Early Cretaceous Na-rich granitoids and their enclaves in the Tengchong Block, SW China: Magmatism in relation to subduction of the Bangong-Nujiang Tethys ocean. *Lithos* **2017**, *286*, 175–190. [CrossRef]
66. Zhang, J.; Peng, T.; Fan, W.; Zhao, G.; Dong, X.; Gao, J.; Peng, B.; Wei, C.; Xia, X.; Chen, L.; et al. Petrogenesis of the Early Cretaceous granitoids and its mafic enclaves in the Northern Tengchong Terrane, southern margin of the Tibetan Plateau and its tectonic implications. *Lithos* **2018**, *314–315*, 283–298. [CrossRef]
67. Qi, X.; Wei, C.; Zhang, C.; Zhang, S.; Hu, Z.; Ji, F. Southward extension of the Bangonghu–Nujiang Suture: Evidence from Early Cretaceous intermediate and felsic magmatism in the Gaoligong Orogen, China. *J. Asian Earth Sci.* **2019**, *182*, 1–25. [CrossRef]
68. Chen, Y.; Li, G.; Qin, L.; Lu, Y.; Jiang, C. Geochronology and geochemistry of Cretaceous–Eocene granites, Tengchong Block (SW China): Petrogenesis and implications for Mesozoic-Cenozoic tectonic evolution of Eastern Tethys. *Geosci. Front.* **2022**, *13*, 101338. [CrossRef]
69. Zhang, J.; Fan, W.; Xu, X.; Peng, T.; Ratschbacher, L.; Wang, B. Early Cretaceous magmatism in Yunnan traces the tectonic transition from the Tengchong-Baoshan continental collision to Neo-Tethyan slab rollback. *Lithos* **2023**, *456*, 106717. [CrossRef]
70. Altherr, R.; Holl, A.; Hegner, E.; Langer, C.; Kreuzer, H. High-potassium, calc-alkaline I-type plutonism in the European Variscides: Northern Vosges (France) and northern Schwarzwald (Germany). *Lithos* **2000**, *50*, 51–73. [CrossRef]
71. Sylvester, P.J. Post-collisional strongly peraluminous granites. *Lithos* **1998**, *45*, 29–44. [CrossRef]
72. Pearce, J.A.; Harris, N.B.W.; Tindle, A.G. Trace element discrimination diagrams for the tectonic interpretation of granitic rocks. *J. Petrol.* **1984**, *25*, 956–983. [CrossRef]
73. Yang, J.; Cawood, P.A.; Du, Y.; Huang, H.; Hu, L. Detrital record of Indosinian mountain building in SW China: Provenance of the Middle Triassic turbidites in the Youjiang Basin. *Tectonophysics* **2012**, *574*, 105–117. [CrossRef]
74. Yang, J.; Cawood, P.A.; Du, Y.; Huang, H.; Huang, H.; Tao, P. Large Igneous Province and magmatic arc sourced Permian–Triassic volcanogenic sediments in China. *Sediment. Geol.* **2012**, *261*, 120–131. [CrossRef]
75. He, X.; Liu, Z.; Wang, G.; Leonard, N.D.; Tao, W.; Tan, S. Petrogenesis and tectonic setting of the Early Cretaceous granitoids in the eastern Tengchong terrane, SW China: Constraint on the evolution of Meso-Tethys. *Lithosphere* **2020**, *12*, 150–165. [CrossRef]
76. Chen, X.; Hu, R.; Bi, X.; Li, H.; Lan, J.; Zhao, C.; Zhu, J. Cassiterite LA-MC-ICP-MS U/Pb and muscovite $^{40}Ar/^{39}Ar$ dating of tin deposits in the Tengchong-Lianghe tin district, NW Yunnan, China. *Miner. Depos.* **2014**, *49*, 843–860. [CrossRef]
77. Zhang, J.; Fan, W.; Peng, T.; Ratschbacher, L. Southeastern continuation of the Bangong-Nujiang suture zone: Constraints from Middle Jurassic–Early Cretaceous sedimentary rocks in the western Baoshan block, SW China. *J. Asian Earth Sci.* **2021**, *212*, 104944. [CrossRef]
78. Zhang, J.; Fan, W.; Peng, T.; Ratschbacher, L. An early cretaceous arc–back-arc system in western Yunnan, SW China: Constraints from U-Pb zircon ages and geochemistry of volcanic rocks in the western Baoshan block. *Lithos* **2022**, *412*, 106555. [CrossRef]
79. Cong, F.; Lin, S.; Zou, G.; Xie, T.; Li, Z.; Tang, F.; Peng, Z. Geochronology and Petrogenesis for the Protolith of Biotite Plagioclase Gneiss at Lianghe, Western Yunnan. *Acta Geol. Sin. (Engl. Ed.)* **2011**, *85*, 891–904. [CrossRef]
80. Deng, J.; Wang, Q.; Li, G.; Li, C.; Wang, C. Tethys tectonic evolution and its bearing on the distribution of important mineral deposits in the Sanjiang region, SW China. *Gondwana Res.* **2014**, *26*, 419–437. [CrossRef]
81. Li, J.; Zhang, L.; Fan, W.; Ding, L.; Sun, Y.; Peng, T.; Li, G.; Sein, K. Mesozoic-Cenozoic tectonic evolution and metallogeny in Myanmar: Evidence from zircon/cassiterite U–Pb and molybdenite Re–Os geochronology. *Ore Geol. Rev.* **2018**, *97*, 829–845. [CrossRef]
82. Mao, W.; Zhong, H.; Yang, J.; Liu, L.; Fu, Y.; Zhang, X.; Doh, S.H. Geochronology of Sn mineralization in Myanmar: Metallogenic implications. *Econ. Geol.* **2022**, *117*, 1387–1403. [CrossRef]
83. Mao, W.; Zhong, H.; Yang, J.; Tang, Y.; Liu, L.; Fu, Y.; Zhang, X.; Sein, K.; Aung, S.M.; Li, J.; et al. Combined Zircon, Molybdenite, and Cassiterite Geochronology and Cassiterite Geochemistry of the Kuntabin Tin-Tungsten Deposit in Myanmar. *Econ. Geol.* **2020**, *115*, 603–625. [CrossRef]

84. Liu, C.; Chung, S.; Wu, F.; Zhang, C.; Xu, Y.; Wang, J.; Chen, Y.; Guo, S. Tethyan suturing in Southeast Asia: Zircon U-Pb and Hf-O isotopic constraints from Myanmar ophiolites. *Geology* **2016**, *44*, 311–314. [CrossRef]
85. Warr, L.N. IMA-CNMNC approved mineral symbols. *Mineral. Mag.* **2021**, *85*, 291–320. [CrossRef]

Disclaimer/Publisher's Note: The statements, opinions and data contained in all publications are solely those of the individual author(s) and contributor(s) and not of MDPI and/or the editor(s). MDPI and/or the editor(s) disclaim responsibility for any injury to people or property resulting from any ideas, methods, instructions or products referred to in the content.